Moiré patterns in doubly differential electron-momentum distributions in atomic ionization by mid-infrared lasers

Martín Dran and Diego G. Arbó*
Institute for Astronomy and Space Physics IAFE (UBA-Conicet), Buenos Aires, Argentina

(Received 14 February 2018; published 15 May 2018)

We analyze the doubly differential electron momentum distribution in above-threshold ionization of atomic hydrogen by a linearly polarized mid-infrared laser pulse. We reproduce side rings in the momentum distribution with forward-backward symmetry previously observed by Lemell *et al.* [Phys. Rev. A **87**, 013421 (2013)], whose origin, as far as we know, has not been explained so far. By developing a Fourier theory of moiré patterns, we demonstrate that such structures stem from the interplay between intra- and intercycle interference patterns which work as two separate grids in the two-dimensional momentum domain. We use a three-dimensional (3D) description based on the saddle-point approximation (SPA) to unravel the nature of these structures. When the periods of the two grids (intra- and intercycle) are similar, principal moiré patterns arise symmetrically as concentric rings in the forward and backward directions at high electron kinetic energy. Higher order moiré patterns are observed and characterized when the period of one grid is multiple of the other. We find a scale law for the position (in momentum space) of the center of the moiré rings in the tunneling regime. We verify the SPA predictions by comparison with time-dependent distorted-wave strong-field approximation calculations and the solutions of the full 3D time-dependent Schrödinger equation.

DOI: 10.1103/PhysRevA.97.053406

I. INTRODUCTION

In a typical photoionization process in the tunneling regime, electrons are emitted by tunneling through the potential barrier formed by the combination of the atomic potential and the external strong field. Tunneling occurs within each optical cycle predominantly around the maxima of the electric field's absolute value. According to the well-known three-step model, photoelectrons can be classified into *direct* and *rescattered* electrons [1–3]. After ionization, direct electrons can escape without being strongly affected by the residual core potential. The classical cutoff energy for this process is twice the ponderomotive energy. After being accelerated back by the laser field, a small portion of electrons are rescattered by the parent ion and can achieve a kinetic energy of up to ten times the ponderomotive energy. Trajectories that correspond to direct ionization are crucial in the formation of interference patterns in photoelectron spectra. Quantum interference within an optical cycle was firstly reported (as far as we know) in Ref. [4] and theoretically analyzed and experimentally observed by Paulus *et al.* in Ref. [5], both for negative ions. A thorough saddle-point analysis with the strong-field approximation can be found in the review of Becker *et al.* [6]. Nonequidistant peaks in the photoelectron spectrum were firstly calculated for neutral atoms by Chirila and Potvliege [7]. A temporal double-slit interference pattern has been studied in near-single cycle pulses both experimentally [8,9] and theoretically [6,10]. Near-threshold oscillations in angular distribution were explained as interferences of electron trajectories [11] and measured by [12]. Diffraction fringes have been experimentally observed in photoionization of He [9,13] and Ne atoms [13] and photodetachment in H^- and [14] F^- ions by femtosecond pulses for fixed frequency [15] and theoretically analyzed [16–19]. Diffraction patterns were also found in spectra of laser-assisted XUV ionization, whose gross structure of sidebands were explained as the interference between electrons emitted within one period [20–24]. The interference pattern in multicycle photoelectron spectra can be identified as a diffraction pattern at a time grating composed of intra- and intercycle interferences [16–19]. While the latter gives rise to the well-known ATI peaks [25–27], the former leads to a modulation of the ATI spectrum in the near-infrared regime offering information on the subcycle ionization dynamics.

In previous papers we analyzed how the interplay between the intercycle interference [factor $B(k)$ in Eq. (25)] and the intracycle interference [factor $F(\vec{k})$ in Eq. (25)] controls the doubly differential distribution of direct above-threshold ionization (ATI) electrons for lasers in the near infrared [17–19]. In a theoretical study about the quantum-classical correspondence in atomic ionization by mid-infrared pulses, Lemell *et al.* calculated the doubly differential momentum distribution after the interaction of a strong mid-infrared laser pulse with a hydrogen atom, which shows multiple peaks and interference structures (see Fig. 1 of [28]). At both sides of the well-known intercycle ATI rings, two distinct ringlike structures appear (symmetrically) in the forward and backward directions. As far as we know, the origin of these structures has not been identified so far. In this paper, we extend the analysis of the saddle-point approximation (SPA) to the mid-infrared regime.

Large-scale interference patterns can be produced when a small-scale grid is overlaid on another similar grid [29,30]. These patterns are named moiré [29,30] and appear in art, physics, mathematics, etc. They show up in everyday life such as a striped shirt seen on television, in the folds of a moving curtain, when looking through parallel wire-mesh fences, etc.

*Corresponding author: diego@iafe.uba.ar

 ©2018 American Physical Society

More than a rareness, moiré is widely used in projection interferometry complementing conventional holographic interferometry, especially for testing optics used at long wavelength. The use of moiré for reduced sensitivity testing was introduced by Lord Rayleigh in 1874 to determine the quality of two identical gratings even though each individual grating could not be resolved under a microscope [31]. Moiré patterns have been extremely useful to help the understanding of basic interferometry and interferometric test results [32–34].

In the present paper, we theoretically investigate the origin of side-ring structures that appear in the doubly differential momentum distribution for atomic ionization by laser pulses in the mid-infrared spectral region [28]. We demonstrate that such structures stem from the interplay between intra- and intercycle interference patterns which work as two separate grids in the two-dimensional momentum domain. When the periods of the two grids (intra- and intercycle) are similar, principal moiré patterns arise as concentric rings at high electron kinetic energy in the forward and backward directions symmetrically. In addition, we show that a whole family of secondary moiré patterns with less visibility than the principal one is also present. We characterize these structures within the Fourier theory of the moiré patterns finding simple scale laws for the position of their center in the momentum distribution. In order to do that, we previously discard the formation of spurious (nonphysical) moiré patterns due to the presence of the numerical grid of the momentum map. We use a three-dimensional (3D) description based on the SPA [17–19] to unravel the nature of these structures. Our SPA predictions are corroborated by comparison with time-dependent distorted-wave strong-field approximation (SFA) [3,7,35–37] calculations and the solutions of the full time-dependent Schrödinger equation (TDSE).

The paper is organized as follows. In the first part of Sec. II, we develop the Fourier theory of moiré patterns. We continue by scheming the semiclassical model for atomic ionization by laser pulses showing that the separation of intracycle and intercycle interferences can be interpreted in terms of diffraction at a time grating when studying the doubly differential distributions within the SPA. In the last part of the section we show how moiré patterns are formed from inter- and intracycle interferences in view of this Fourier theory. In Sec. III, we analyze the ringlike structures in the doubly differential momentum distribution within the SPA and compare them with the SFA and TDSE *ab initio* calculations. We also characterize the moiré structure by analyzing the dependence of the position of the center as a function of laser parameters finding a scale law. Atomic units are used throughout the paper, except when otherwise stated.

II. THEORY

A. Fourier theory of moiré patterns

We define a one-dimensional (1D) grating (vertical stripes) as a periodic function $G(x')$, where p is the period of the grating. Due to its periodicity, the function $G(x')$ can be thought as a sum of different harmonic terms of discrete frequency,

$$G(x') = \sum_{n=-\infty}^{\infty} a_n \exp[i2\pi n f_0 x'], \tag{1}$$

where a_n is the Fourier coefficient and $f_0 = p^{-1}$.

Gratings with a general geometrical layout can be considered as extended coordinate-transformed structures which can be obtained by applying geometric transformations to a standard 1D grating. By replacing x' with a certain function $T(x,y)$, the 1D grating of Eq. (1) can be transformed into another curvilinear grating $G_T(x,y) = G[T(x,y)]$. Therefore, in the same way, the latter can be expressed as

$$G_T(x,y) = \sum_{n=-\infty}^{\infty} a_n \exp[i2\pi n f_0 T(x,y)]. \tag{2}$$

Moiré fringes appear in the overlay of repetitive structures and vary in terms of the geometrical layout of two (or more) superposed structures. The two gratings with the extended layout can be obtained by applying the transformations $T_1(x,y)$ and $T_2(x,y)$ to two 1D gratings of frequencies f_1 and f_2, respectively. The generalized gratings can be expressed as in Eq. (2):

$$G_1(x,y) = \sum_{n=-\infty}^{\infty} a_n \exp[i2\pi n f_1 T_1(x,y)], \tag{3a}$$

$$G_2(x,y) = \sum_{m=-\infty}^{\infty} b_m \exp[i2\pi m f_2 T_2(x,y)]. \tag{3b}$$

The two superimposed gratings can be written as the multiplication of the two general gratings G_1 and G_2, in respective Eqs. (3a) and (3b):

$$\begin{aligned} G(x,y) &= G_1(x,y)G_2(x,y) \\ &= \sum_{n=-\infty}^{\infty}\sum_{m=-\infty}^{\infty} a_n b_m \exp\{i2\pi[nf_1T_1(x,y) \\ &\quad + mf_2T_2(x,y)]\}. \end{aligned} \tag{4}$$

From Eq. (4), we can extract the partial sum $\sum_{n=-\infty}^{\infty}\sum_{m=-\infty}^{\infty} a_n b_m(\cdots) \to \sum_{j=-\infty}^{\infty} a_{jk_1} b_{jk_2}(\cdots)$, with k_1 and k_2 integer numbers different from zero, where we have renamed $n = jk_1$ and $m = jk_2$ [38]. Then, we express this partial sum in the same way as in Eq. (2), namely,

$$\begin{aligned} \tilde{G}_{k_1,k_2}(x,y) = \sum_{j=-\infty}^{\infty} a_{jk_1} b_{jk_2} \exp\{i2\pi jf[k_1(f_1/f)T_1(x,y) \\ + k_2(f_2/f)T_2(x,y)]\}, \end{aligned} \tag{5}$$

where f is a standardized frequency. In this way, the twofold sum of Eq. (4) can be decomposed into many partial sums. The partial sum $\tilde{G}_{k_1,k_2}(x,y)$ does not reproduce the function $G(x,y)$ of Eq. (4) fully since it is simpler than the latter. Thus, there is no one-to-one relation between $\tilde{G}_{k_1,k_2}(x,y)$ and $G(x,y)$. Equation (5) can be regarded as the transformation of a 1D grating with a compound transformation function

$$T_{k_1,k_2}(x,y) = k_1\left(\frac{f_1}{f}\right)T_1(x,y) + k_2\left(\frac{f_2}{f}\right)T_2(x,y), \tag{6}$$

applied to the 1D grating

$$\tilde{G}_{k_1,k_2}(x') = \sum_{j=-\infty}^{\infty} a_{jk_1} b_{jk_2} \exp(i2\pi jf x'). \tag{7}$$

For every pair (k_1,k_2), the partial sum in Eq. (7) converges to a periodic-distributed pattern similar to the layout of standard 1D gratings. By transforming the partial sum of Eq. (7) with the transformation function of Eq. (6), we get the (k_1,k_2)-order moiré pattern of Eq. (5). Summing up, we can say that two geometrically transformed 1D gratings exhibit equivalent patterns to the one obtained by application of a compound transformation to a certain 1D-distributed moiré pattern.

In general, moiré fringes generated by two superposed gratings are transformed from two standard 1D gratings with different frequencies by different transformations. However, in the following section, we restrict our investigation to the special case of moiré fringes generated from 1D gratings with the same frequency, i.e., $f_1 = f_2 = f$, and different transformations, i.e., $T_1(x,y) \neq T_2(x,y)$. Therefore, the moiré pattern of Eq. (5) can be written as

$$\tilde{G}_{k_1,k_2}(x,y) = \sum_{j=-\infty}^{\infty} a_{jk_1} b_{jk_2} \exp\{i2\pi jf[k_1 T_1(x,y) + k_2 T_2(x,y)]\}. \quad (8)$$

The lowest frequency pattern corresponds to the pair $(k_1,k_2) = (1,-1)$, which is usually the most visible one. We name pair $(1,-1)$ as the principal moiré pattern with transformation $T_{1,-1}(x,y) = T_1(x,y) - T_2(x,y)$. Higher order or secondary moiré patterns are also present with less visibility. Later, we will see how the side-ring structure can be thought of as the principal moiré pattern arising from the superposition of intra- and intercycle interferences, each considered as a separate grid G_1 and G_2. Previous to this, in the next subsection, we pose the semiclassical theory of inter- and intracycle interference in the electron yield after atomic ionization by a short laser pulse.

B. Semiclassical model

In this subsection we repeat the theory of the semiclassical model for atomic ionization in the single active electron approximation interacting with a linearly polarized laser field $\vec{F}(t)$ firstly posed in Refs. [17–19]. The reader familiar with the semiclassical model can skip this subsection and go directly to the analysis of the formation of the moiré patterns in the next subsection.

The Hamiltonian of the system in the length gauge is

$$H = \frac{\vec{p}^{\,2}}{2} + V(r) + \vec{r}\cdot\vec{F}(t), \quad (9)$$

where $V(r)$ is the atomic central potential and $\vec{p}$ and $\vec{r}$ are the momentum and position of the electron, respectively. The term $\vec{r}\cdot\vec{F}(t)$ couples the initial state $|\phi_i\rangle$ to the continuum final state $|\phi_f\rangle$ with momentum $\vec{k}$ and energy $E = k^2/2$. The TDSE for the Hamiltonian of Eq. (9) governs the evolution of the electronic state $|\psi(t)\rangle$. We calculate the photoelectron momentum distributions as

$$\frac{dP}{d\vec{k}} = |T_{if}|^2, \quad (10)$$

where T_{if} is the T-matrix element corresponding to the transition $\phi_i \to \phi_f$.

The transition amplitude within the time-dependent distorted-wave theory in the SFA in the *post* form is expressed as [39]

$$T_{if} = -i\int_{-\infty}^{+\infty} dt\langle\chi_f^-(t)|z\,F(t)|\phi_i(t)\rangle, \quad (11)$$

where $\chi_f^-(t)$ is the final distorted-wave function and the initial state $\phi_i(t)$ is an eigenstate of the atomic Hamiltonian without perturbation with eigenenergy equal to minus the ionization potential I_p. If we choose the Hamiltonian of a free electron in the time-dependent electric field as the exit-channel distorted Hamiltonian, i.e., $i\frac{\partial}{\partial t}|\chi_f^-(t)\rangle = [\frac{p^2}{2} + zF(t)]|\chi_f^-(t)\rangle$, the solutions are the Volkov states [40]

$$\chi_{\vec{k}}^{(V)-}(\vec{r},t) = \frac{\exp[i(\vec{k}+\vec{A})\cdot\vec{r}]}{(2\pi)^{3/2}}\exp[iS(t)], \quad (12)$$

where S denotes the Volkov action

$$S(t) = -\int_t^{\infty} dt'\left[\frac{[\vec{k}+\vec{A}(t')]^2}{2} + I_p\right]. \quad (13)$$

In Eqs. (12) and (13), $\vec{A}(t) = -\int_{-\infty}^{t} dt'\vec{F}(t')$ is the vector potential of the laser field divided by the speed of light. Equation (11) together with Eq. (12) leads to the SFA transition matrix. Accordingly, the influence of the atomic core potential on the continuum state of the receding electron is neglected and, therefore, the momentum distribution is a constant of motion after conclusion of the laser pulse [3,41].

To solve the time integral in Eq. (11), we closely follow the SPA [3,7,37,42], which considers the transition amplitude as a coherent superposition of electron trajectories

$$T_{if}(\vec{k}) = -\sum_{i=1}^{M} G(t_r^{(i)},\vec{k})e^{iS(t_r^{(i)})}. \quad (14)$$

Here, M is the number of trajectories born at ionization times $t_r^{(i)}$ reaching a given final momentum $\vec{k}$, and $G(t_r^{(i)},\vec{k})$ is the ionization amplitude,

$$G\left(t_r^{(i)},\vec{k}\right) = \left[\frac{2\pi i F\left(t_r^{(i)}\right)}{\left|\vec{k}+\vec{A}\left(t_r^{(i)}\right)\right|}\right]^{1/2} d^*\left[\vec{k}+\vec{A}\left(t_r^{(i)}\right)\right], \quad (15)$$

where $d^*(\vec{v})$ is the dipole element of the bound-continuum transition.

The release time $t_r^{(i)}$ of trajectory i is determined by the saddle-point equation,

$$\left.\frac{\partial S(t')}{\partial t'}\right|_{t'=t_r^{(i)}} = \frac{\left[\vec{k}+\vec{A}\left(t_r^{(i)}\right)\right]^2}{2} + I_p = 0, \quad (16)$$

yielding complex values since $I_p > 0$. The condition for different trajectories to interfere is to reach the same final momentum $\vec{k}$ to satisfy Eq. (16) with release times $t_r^{(i)}$ $(i = 1,2,\ldots,M)$. Whereas the interference condition involves the vector potential $\vec{A}$, the electron trajectory is governed by the electrical field $\vec{F}$. We now consider a periodic laser linearly polarized along the z axis whose laser field is $\vec{F}(t) = F_0\hat{z}\sin(\omega t)$, where F_0 is the field amplitude. Accordingly, the vector potential is given by $\vec{A}(t) = \frac{F_0}{\omega}\hat{z}\cos(\omega t)$. There are two solutions of Eq. (16) per optical cycle. The first solution in the jth cycle is given by

$$t_r^{(j,1)} = \frac{2\pi(j-1)}{\omega} + \frac{1}{\omega}\cos^{-1}[-\tilde{\kappa}], \quad (17)$$

where $\tilde{\kappa}$ denotes the complex final momentum defined by

$$\tilde{\kappa} = \kappa_z + i\sqrt{\gamma^2 + \kappa_\perp^2}, \tag{18}$$

and κ_z and $\kappa_\perp$ are the respective longitudinal and transversal components of the dimensionless scaled final momentum of the electron $\vec{\kappa} = \omega\vec{k}/F_0$. In Eq. (18) $\gamma = \sqrt{2I_p}\,\omega/F_0$ is the Keldysh parameter. The second solution fulfills

$$t_r^{(j,2)} = \begin{cases} \frac{4\pi}{\omega}\left(j - \frac{1}{2}\right) - t_r^{(j,1)} & \text{if} \quad \kappa_z \geqslant 0 \\ \frac{4\pi}{\omega}(j-1) - t_r^{(j,1)} & \text{if} \quad \kappa_z < 0. \end{cases} \tag{19}$$

In Eqs. (17) and (19), $t_r^{(j,\alpha)}$ with $\alpha = 1$ (2) denotes the early (late) release times within the jth cycle.

For a given value of $\vec{k}$, the field strength for ionization at $t_r^{(j,\alpha)}$ is independent of j and α, then $|F(t_r^{(j,\alpha)})| = F_0|\sqrt{1-\tilde{\kappa}^2}|$. The ionization rate $\Gamma(\vec{k}) = |G(t_r^{(j,\alpha)},\vec{k})|^2 e^{-2\mathrm{Im}[S(t_r^{(j,\alpha)})]}$ is identical for all subsequent ionization bursts (or trajectories) and, therefore, only a function of the time-independent final momentum $\vec{k}$ provided the ground-state depletion is negligible. As there are two interfering trajectories per cycle, the total number of interfering trajectories with final momentum $\vec{k}$ is $M = 2N$, with N being the number of cycles involved in the laser pulse. Hence, the sum over interfering trajectories [Eq. (14)] can be decomposed into those associated with two release times within the same cycle and those associated with release times in different cycles [17–19]. Consequently, the momentum distribution [Eq. (10)] can be written within the SPA as

$$\frac{dP}{d\vec{k}} = \Gamma(\vec{k})\left|\sum_{j=1}^{N}\sum_{\alpha=1}^{2} e^{i\,\mathrm{Re}[S(t_r^{(j,\alpha)})]}\right|^2, \tag{20}$$

where the second factor on the right-hand side of Eq. (20) describes the interference of $2N$ trajectories with final momentum $\vec{k}$, where $t_r^{(j,\alpha)}$ is a function of $\vec{k}$ through Eqs. (17) and (19).

The semiclassical action along one electron trajectory with release time $t_r^{(j,\alpha)}$ can be calculated within the SPA from Eq. (13) up to a constant,

$$S\left(t_r^{(j,\alpha)}\right) = 2U_p\left[\left(|\tilde{\kappa}|^2 + \frac{1}{2}\right)t_r^{(j,\alpha)} + \frac{\sin\left(2\omega t_r^{(j,\alpha)}\right)}{4\omega} + 2\frac{\kappa_z}{\omega}\sin\left(\omega t_r^{(j,\alpha)}\right)\right], \tag{21}$$

where the ponderomotive energy is given by $U_p = F_0^2/4\omega^2$, and $|\tilde{\kappa}|^2 = |\vec{\kappa}|^2 + \gamma^2$ [see Eq. (18)]. The sum in Eq. (20) can be written as

$$\sum_{j=1}^{N}\sum_{\alpha=1}^{2} e^{i\mathrm{Re}[S(t_r^{(j,\alpha)})]} = 2\sum_{j=1}^{N} e^{i\bar{S}_j}\cos\left(\frac{\Delta S_j}{2}\right), \tag{22}$$

where $\bar{S}_j = \mathrm{Re}[S(t_r^{(j,1)}) + S(t_r^{(j,2)})]/2$ is the average action of the two trajectories released in cycle j, and $\Delta S_j = \mathrm{Re}[S(t_r^{(j,1)}) - S(t_r^{(j,2)})]$ is the accumulated action between the two release times $t_r^{(j,1)}$ and $t_r^{(j,2)}$ within the same jth cycle. The average action depends linearly on the cycle number j, so $\bar{S}_j = S_0 + j\tilde{S}$, where S_0 is a constant which will drop out when the absolute value of Eq. (22) is taken, and

$$\tilde{S} = (2\pi/\omega)(E + U_p + I_p). \tag{23}$$

In turn, due to discrete translation invariance in the time domain ($t \to t + 2j\pi/\omega$), the difference of the action ΔS_j is independent of the cycle number j, which can be expressed (dropping the subscript j) as

$$\Delta S = \frac{-2U_p}{\omega}\,\mathrm{Re}[(1 + 2|\tilde{\kappa}|^2)\mathrm{sgn}(\kappa_z)\cos^{-1}[\mathrm{sgn}(\kappa_z)\tilde{\kappa}] - (4\kappa_z - \tilde{\kappa})\sqrt{1-\tilde{\kappa}^2}], \tag{24}$$

where sgn denotes the sign function that accounts for positive and negative longitudinal momentum k_z.

After some algebra, Eq. (20) can be rewritten as an equation of a diffraction grating of the form [17–19,43,44]

$$\frac{dP}{d\vec{k}} = 4\,\Gamma(\vec{k})\underbrace{\cos^2\left(\frac{\Delta S}{2}\right)}_{F(\vec{k})}\underbrace{\left[\frac{\sin(N\tilde{S}/2)}{\sin(\tilde{S}/2)}\right]^2}_{B(k)}, \tag{25}$$

where the interference pattern can be factorized into two contributions: (i) the interference stemming from a pair of trajectories within the same cycle (intracycle interference), governed by $F(\vec{k})$ and (ii) the interference stemming from trajectories released at different cycles (intercycle interference) resulting in the well-known ATI peaks given by $B(k)$ (see Ref. [45]). The intracycle interference arises from the superposition of pairs of trajectories separated by a time slit $\Delta t = t_r^{(j,1)} - t_r^{(j,2)}$ of the order of less than half a period of the laser pulse, i.e., $\mathrm{Re}(\Delta t) < \pi/\omega$, while the difference between $t_r^{(j,\alpha)}$ and $t_r^{(j+1,\alpha)}$ is $2\pi/\omega$, i.e., the optical period of the laser. It is worth noting that whereas the intracycle factor $F(\vec{k})$ depends on the angle of emission, the intercycle factor $B(k)$ depends only on the absolute value of the final momentum (or energy). Equation (25) may be viewed as a diffraction grating in the time domain consisting of N slits with an interference factor $B(k)$ and diffraction factor $F(\vec{k})$ for each slit. In the following subsection we make use of the Fourier theory of the last subsection to analyze the moiré patterns in the doubly differential momentum distribution [Eq. (25)].

C. Formation of moiré patterns from inter- and intracycle interference

The intercycle principal maxima fulfill the equation $\tilde{S} = 2n\pi$, leading to the ATI energies $E_n = n\omega - U_p - I_p$ in agreement with the conservation of energy for the absorption of n photons. Therefore, in the doubly differential momentum distribution, the two-dimensional (2D) intercycle grid follows the relation between the parallel and perpendicular momenta $k_\perp^{\mathrm{inter}}(n) = \sqrt{2(n\omega - I_p - U_p) - [k_z^{\mathrm{inter}}(n)]^2}$. The spacing between two consecutive maxima can be easily calculated for $E_n = k_z^2/2$ (provided $k_\perp = 0$) as

$$\frac{\left[k_z^{\mathrm{inter}}(n+1)\right]^2 - \left[k_z^{\mathrm{inter}}(n)\right]^2}{2} \simeq k_z\Delta k_z^{\mathrm{inter}} \Rightarrow \Delta k_z^{\mathrm{inter}} \simeq \frac{\omega}{k_z} = \frac{1}{\alpha\,\kappa_z}, \tag{26}$$

where $\alpha = 4U_p/F_0 = F_0/\omega^2$ is the quiver amplitude of the escaping electron, $\vec{\kappa} = (\omega/F_0)\vec{k}$; and in the last line we have used that $E_{n+1} - E_n = \omega$.

The intracycle maxima correspond to the equation $\Delta S = 2m\pi$ with integer m. Equivalently to the intercycle case, the intracycle spacing can be calculated as

$$\frac{\Delta S(k_z + \Delta k_z)}{2} - \frac{\Delta S(k_z)}{2} \simeq \frac{1}{2}\frac{\partial \Delta S(k_z)}{\partial k_z}\bigg|_{k_\perp=0} \Delta k_z^{\text{intra}} \Rightarrow \Delta k_z^{\text{intra}} \simeq \frac{2\pi}{\left|\frac{\partial \Delta S(k_z)}{\partial k_z}\right|_{k_\perp=0}}. \tag{27}$$

After a bit of algebra, the derivative of the accumulated action with respect to the parallel momentum can be written in a close form and, thus, the intracycle spacing reads

$$\Delta k_z^{\text{intra}} = \frac{\pi}{\alpha|\text{Re}[\kappa_z \cos^{-1}(\kappa_z + i\gamma) - \sqrt{1-(\kappa_z+i\gamma)^2}]|}. \tag{28}$$

In Eq. (28) we have considered forward emission, i.e., $k_z \geqslant 0$. We have an analogous result for backward emission.

According to Eq. (25), the transformations from the 1D grating to the inter- and intracycle 2D grating are $T_1(k_z,k_\perp) = \tilde{S}/2$ given by Eq. (23) and $T_2(k_z,k_\perp) = \Delta S/2$ given by Eq. (24). Therefore, we can write the (k_1,k_2)-order compound transformation $T(k_z,k_\perp) = k_1 T_1(k_z,k_\perp) + k_2 T_2(k_z,k_\perp)$ as

$$T(k_z,k_\perp) = k_1\frac{\tilde{S}}{2} + k_2\frac{\Delta S}{2}. \tag{29}$$

By eye inspection [at least for the lowest orders $(k_1,k_2) = (1,-1)$, $(2,-1)$, and $(1,-2)$] function $T(k_z,k_\perp)$ exhibits one global minimum for forward (and backward) emission, which corresponds to the center of the side ring. The minimum can be easily found as

$$\vec{\nabla} T(k_z,k_\perp) = \left(\frac{\partial T(k_z,k_\perp)}{\partial k_z}, \frac{\partial T(k_z,k_\perp)}{\partial k_\perp}\right) = 0. \tag{30}$$

$k_\perp = 0$ is a solution of $\partial\tilde{S}/\partial k_\perp = 0$ and $\partial\Delta S/\partial k_\perp = 0$, separately, and independently of the value of k_z. Therefore, $k_\perp = 0$ is a solution of the second component of Eq. (30), $\partial T(k_z,k_\perp)/\partial k_\perp = (k_1/2)(\partial\tilde{S}/\partial k_\perp) + (k_2/2)(\partial\Delta S/\partial k_\perp) = 0$, irrespective of the values of k_1, k_2, and k_z. This means that the center of the moiré rings lay along the k_z axis ($k_\perp = 0$).

Now, with the restriction $k_\perp = 0$, we formally solve the first component of Eq. (30),

$$\frac{\partial T(k_z,k_\perp)}{\partial k_z} = \frac{k_1}{2}\frac{\partial\tilde{S}}{\partial k_z} + \frac{k_2}{2}\frac{\partial\Delta S}{\partial k_z} = 0. \tag{31}$$

The derivative in the first term in the right -hand side of Eq. (31) can be easily written as $\partial\tilde{S}/\partial k_z = 2\pi k_z/\omega = 2\pi/\Delta k_z^{\text{inter}}$, where we have used Eqs. (23) and (26). Doing the same with the derivative in the second term of Eq. (31), we get that $\partial\Delta S/\partial k_z = 2\pi/\Delta k_z^{\text{intra}}$, using Eq. (27). Therefore, Eq. (31) can be written as

$$\frac{\partial T(k_z,k_\perp)}{\partial k_z} = \pi\left(\frac{k_1}{\Delta k_z^{\text{inter}}} + \frac{k_2}{\Delta k_z^{\text{intra}}}\right) = 0, \tag{32}$$

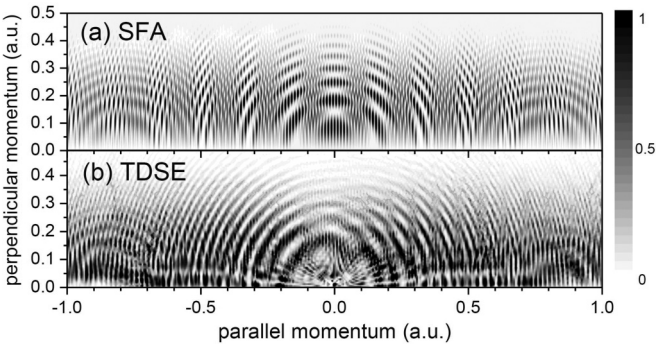

FIG. 1. Momentum distributions (linear gray scale) after interaction of a mid-infrared laser pulse with a hydrogen atom. (a) SFA and (b) TDSE [28,46]. The cosinelike pulse has a peak field $F_0 = 0.0533$ ($I = 10^{14}$ W/cm^2), frequency $\omega = 0.014\,24$ ($\lambda = 3200$ nm) and a sin^2 envelope with total pulse duration of eight cycles. Both distributions have been normalized.

which is equivalent to

$$k_1\Delta k_z^{\text{intra}} = -k_2\Delta k_z^{\text{inter}}. \tag{33}$$

The principal moiré rings are given by the lowest order $(k_1,k_2) = (1,-1)$, which means that the intra- and intercycle spacings should be the same, i.e., $\Delta k_z^{\text{intra}} = \Delta k_z^{\text{inter}}$. This result provides the position of the center of the principal moiré pattern. Higher order moiré patterns, i.e., $(k_1,k_2) = (2,-1)$ and $(1,-2)$, denote the secondary moiré rings whose centers are positioned along the k_z axis at the k_z value which makes the intercycle spacing the double of the intracycle one, i.e., $2\Delta k_z^{\text{intra}} = \Delta k_z^{\text{inter}}$, and the intracycle spacing the double of the intercycle one, i.e., $\Delta k_z^{\text{intra}} = 2\Delta k_z^{\text{inter}}$, respectively.

In order to discard possible artifacts or spurious (nonphysical) patterns generated by the grating inherent to the data grid, we have analyzed the moiré patterns stemming from the interplay between the intercycle factor $B(k)$ and the numerical grid. When the numerical spacing is much lower than the intercycle spacing there is no formation of moiré rings (not shown). The same can be done with the intracycle pattern. In all our figures in the paper, the numerical grid is much denser than the inter- and intracycle grids, avoiding, in this way, the formation of nonphysical moiré patterns.

III. RESULTS AND DISCUSSION

In Figs. 1(a) and 1(b) we show the doubly differential electron momentum distribution within the SFA [Eqs. (10) and (11)] and TDSE [28,46] after ionization of atomic hydrogen by an intense ($I = 10^{14}$ W/cm^2) mid-infrared ($\lambda = 3200$ nm or equivalently $\omega = 0.01424$ a.u.) sine pulse of eight-cycle total duration with a sin^2 envelope. The intercycle pattern appears as concentric (ATI) rings centered at the threshold. In the TDSE momentum distribution, the characteristic bouquet-shape structure due to interference of electron trajectories oscillating about the Kepler trajectory is clearly observed [11,47]. The bouquet-shape structure is absent in the SFA since it lacks the effect of the Coulomb potential on the escaping trajectories. At both sides of the ATI rings, two symmetrical annular structures at $|k_z| \simeq 0.82$ are observed in both (SFA and

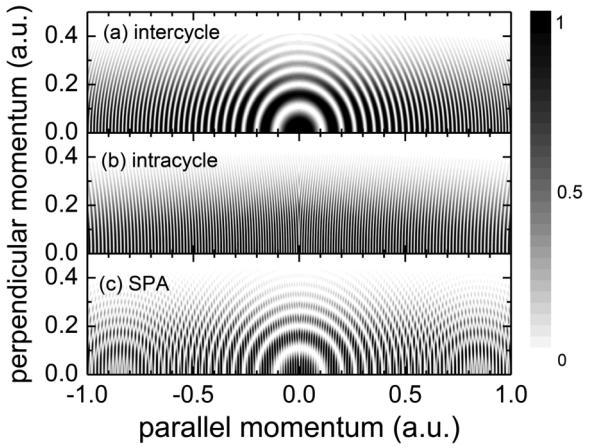

FIG. 2. SPA doubly differential momentum distribution (linear gray scale) of Eq. (25). (a) Intercycle interference: $4\Gamma(\vec{k})F(\vec{k})$; (b) intracycle interference: $4\Gamma(\vec{k})B(k)$ for $N=2$ cycles; and (c) total (intra- and intercycle) interference $4\Gamma(\vec{k})F(\vec{k})B(k)$ for $N=2$ cycles. The laser parameters are $F_0=0.0533$ ($I=10^{14}$ W/cm^2) and frequency $\omega=0.01424$ ($\lambda=3200$ nm). Distributions have been normalized.

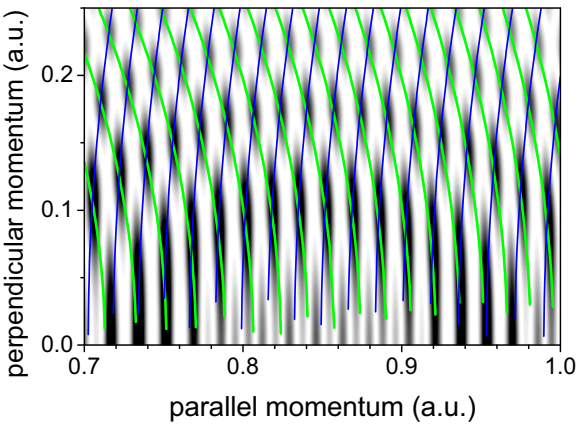

FIG. 3. Magnification of SPA doubly differential momentum distribution in Fig. 2(c) (linear gray scale). On top of it we have drawn the different intercycle maxima, i.e., $\tilde{S}=2n\pi$ (with integer n) in green (gray) and the different intracycle interference maxima, i.e., $\Delta S=2m\pi$ (with integer m) in blue (black). The local maxima of the doubly differential momentum distribution coincide with the intersection of the inter- and intracycle maxima.

TDSE) approaches. As far as we know, the physical nature of these side rings has not been studied. As the SFA does not consider rescattering electrons, we must discard this effect as a possible explanation for the formation of the side rings. In the rest of the paper we identify the origin of these rings with the aid of the semiclassical model and the theory of moiré patterns.

The interplay between the intercycle interference [factor $B(k)$ in Eq. (25)] and the intracycle interference [factor $F(\vec{k})$ in Eq. (25)] controls the doubly differential distribution of direct ATI electrons for lasers [17–19]. Firstly, we examine the intercycle interference within the SPA by setting the intracycle factor to be $F(\vec{k})=1$ in Eq. (25) for the same laser parameters as in Fig. 1, except the duration and envelope, where we use $N=2$ cycles of duration. The factor $B(k)$ reduces to the two-slit Young interference expression $B(k)=4\cos^2[\pi/\omega(\tilde{S}/2)]$, where $\tilde{S}$ is given by Eq. (23). We plot the corresponding SPA doubly differential momentum distribution in Fig. 2(a), where we can observe concentric rings with radii $k_n=\sqrt{2E_n}$. The intracycle interference arises from the superposition of two trajectories released within the same optical cycle, i.e., $\alpha=1,2$ and $N=1$ in Eq. (25) or, equivalently, $4\,\Gamma(\vec{k})F(\vec{k})$, since $B(k)=1$ in this case. In Fig. 2(b), we see that the SPA intracycle interference pattern gives approximately vertical thin stripes which bend to the higher energy region as the transverse momentum grows. The width of the stripes increases with the energy. In order to analyze the complete pattern stemming from all four interfering trajectories in the two-cycle pulse, the composition of the intercycle and intracycle interference patterns of Figs. 2(a) and 2(b) gives the SPA momentum distribution of Fig. 2(c). We can see that a grosser structure emerges as two side rings centered at $k_z\simeq\pm0.83$ and $k_\perp\simeq0$, and two less visible rings centered at $k_z\simeq\pm0.5$ and $k_\perp\simeq0$. If we consider longer pulses, the contrast of intercycle factor $B(k)$ will grow as N will increase. For example, the ATI rings will become narrower and $N-2$ secondary rings will appear between two consecutive principal ATI rings. On the other hand, the intracycle factor $F(\vec{k})$ is independent of the number of cycles N involved in the laser pulse and, in consequence, the intracycle interference pattern remains unchanged. This is strictly valid provided we consider a flattop pulse in the SPA. Moreover, we have checked that the position of the side rings is independent of the pulse duration (not shown).

In Fig. 3, we show in green (gray) the maxima of the intercycle interference pattern, i.e., $\tilde{S}=2n\pi$ with n integer, given by the conservation of energy relation, and in blue (black) the maxima of the intracycle interference pattern, i.e., $\Delta S=2m\pi$ with m integer, on top of the SPA doubly differential momentum distribution of Fig. 2(c) in the region of the main side ring in the forward direction. We clearly see how the intersections of the inter- and intracycle grids coincide with the different local maxima of the distribution forming an annular structure. Contrarily to the intercycle grid, the intracycle grid does not have an explicit form and must be solved numerically.

In Fig. 4(a) we show a close-up of the SPA doubly differential momentum distribution for the same laser parameters as in Figs. 2 and 3. The side ring centered at $(k_z,k_\perp)\simeq(0.83,0)$ is clearly seen. In Fig. 3(b) we plot the principal moiré ring, i.e., $\cos^2[T(k_z,k_\perp)]$, where the transformation $T(k_z,k_\perp)$ is given by Eq. (29) for $(k_1,k_2)=(1,-1)$. We see that the shape and position of the moiré pattern in Fig. 4(b) coincide with the side ring of the doubly differential momentum distribution in Fig. 4(a). When the laser frequency is increased to $\omega=0.02$, the principal side ring shifts horizontally toward less energetic domains and is centered at $(k_z,k_\perp)\simeq(0.62,0)$, as can be observed in Fig. 4(c). The corresponding moiré pattern in Fig. 4(d), also shifts accurately reproducing the side ring. This is a confirmation of the application of the principal moiré patterns theory to atomic ionization in the mid-infrared range posed in the last section.

To fully confirm the theory of the moiré patterns, we plot the inter- and intracycle spacings for $\omega=0.014\,24$ in Fig. 5(a) and $\omega=0.02$ in Fig. 5(b) in a solid line, together with the

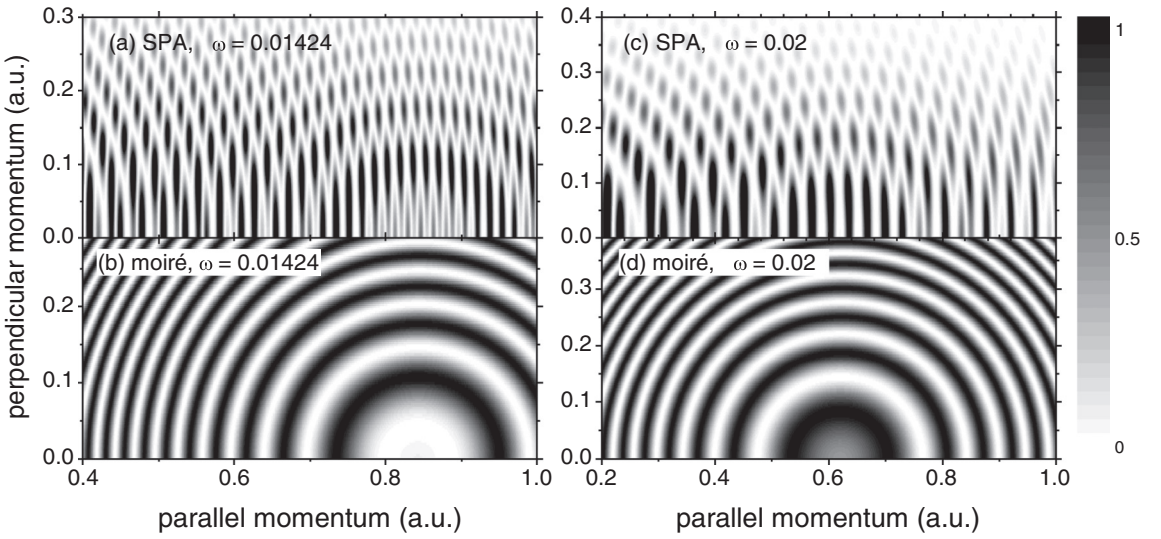

FIG. 4. SPA doubly differential momentum distribution (linear gray scale) of Eq. (25) [(a) and (c)] and the corresponding $(1,-1)$ moiré pattern [(b) and (d)]. The laser frequency is $\omega = 0.01424$ for (a) and (b) and $\omega = 0.02$ for (c) and (d). The rest of the laser parameters are the same as in Figs. 2 and 3. Distributions have been normalized.

double of the corresponding spacings in dashed lines. The rest of the laser parameters are the same as in previous figures. In the second row of Fig. 5 the principal moiré ring is centered at the k_z value, which corresponds to the intersection of the inter- and intracycle spacings in agreement with Eq. (33) for $(k_1,k_2) = (1,-1)$, i.e., $\Delta k_z^{\rm intra} = \Delta k_z^{\rm inter}$. We see that the center of the moiré pattern is situated at $k_z = 0.84$ for $\omega = 0.014\,24$ in Fig. 5(b), whereas it is at $k_z = 0.62$ for $\omega = 0.02$ in Fig. 5(g). In the third row we see that the secondary moiré pattern of order $(2,-1)$ is centered at the intersection of the intercycle spacing

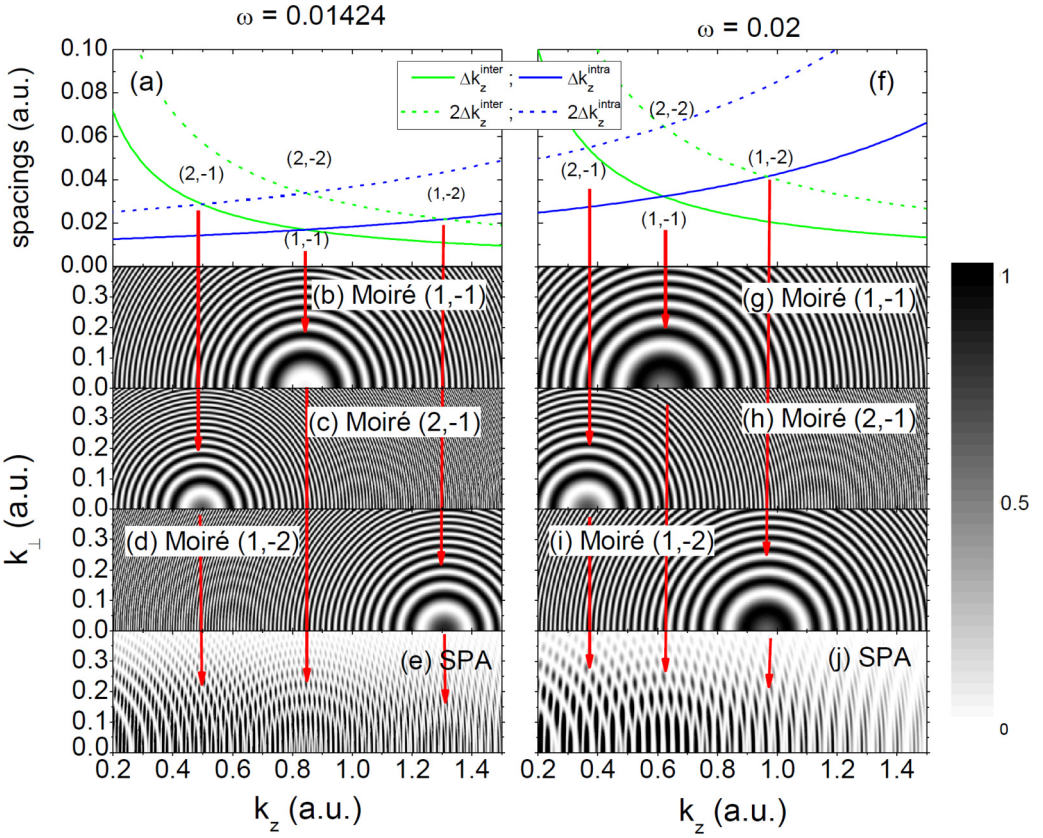

FIG. 5. Inter- and intracycle spacings with their first harmonic (twice the spacings) of Eqs. (26) and (28), respectively [(a) and (f)]. Main moiré $(1,-1)$ pattern [(b) and (g)] and secondary moiré $(1,-2)$ [in (c) and (h)] and $(2,-1)$ [in (d) and (i)] patterns. SPA doubly differential momentum distribution (linear gray scale) of Eq. (25) in (e) and (j). For the first column (a)–(e) $\omega = 0.01424$ and for the second column (f)–(j) $\omega = 0.02$. The rest of the laser parameters are the same as in Figs. 2–4. Distributions have been normalized.

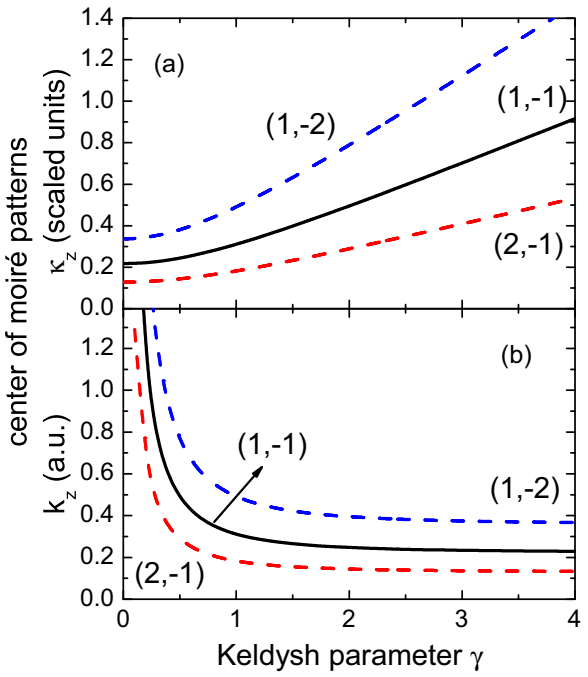

FIG. 6. Position of the center of the main and secondary moiré patterns in units of the scaled parallel momentum κ_z (a) and the parallel momentum k_z (b) as a function of the Keldysh parameter γ.

and twice the intracycle spacing in agreement with Eq. (33), i.e., $2\Delta k_z^{\text{intra}} = \Delta k_z^{\text{inter}}$. The center of the $(2,-1)$ is at $k_z = 0.5$ for $\omega = 0.014\,24$ in Fig. 5(c), whereas it is at $k_z = 0.37$ for $\omega = 0.02$ in Fig. 5(h). In the fourth line we see that the secondary moiré pattern of order $(1,-2)$ is centered at the intersection of twice the intercycle spacing and the intracycle spacing in agreement with Eq. (33), i.e., $\Delta k_z^{\text{intra}} = 2\Delta k_z^{\text{inter}}$. The center of the $(1,-2)$ is at $k_z = 1.31$ for $\omega = 0.014\,24$ in Fig. 5(d), whereas it is at $k_z = 0.97$ for $\omega = 0.02$ in Fig. 5(i). For the sake of completeness, in the last row, we show the complete doubly differential momentum distribution within the SPA. We clearly observe how the principal $(1,-1)$ and secondary $(2,-1)$ and $(1,-2)$ moiré patterns are mirrored in the momentum distribution. Not only does the center of the moiré rings coincide with the prediction of Eq. (33) and observed in the corresponding moiré patterns $\cos^2[(T(k_z,k_\perp)]$, but also the radii of the moiré rings perfectly agree with the momentum distribution. We want to point out that not only are the positions of the center of the moiré structures described by the theory but also the radii of the rings themselves are fully reproduced. No counterpart of the secondary moiré rings $(2,-1)$ and $(1,-2)$ are observed in the SFA and TDSE doubly differential momentum distribution of Fig. 1 since their visibility is very poor. In conclusion, Fig. 5 provides a full confirmation of the application of the theory of the moiré patterns for principal and secondary rings to the formation of the side rings in the ionization of atomic hydrogen by mid-infrared lasers.

From Eqs. (26) and (28) we see that the positions of the centers of the principal and secondary rings in terms of κ_z do not depend on the laser amplitude F_0 and frequency ω independently, but through the Keldysh parameter γ. With this in mind, in Fig. 6 we plot the center of the principal $(1,-1)$ and secondary $(2,-1)$ and $(1,-2)$ moiré rings as a function of γ. In Fig. 6(a), we observe that the position of the center of both principal and secondary rings measured in terms of the scaled κ_z momentum increases with the Keldysh parameter. In the tunneling limit ($\gamma \ll 1$), the position of the center of the moiré rings approaches to constant values $\kappa_{zc}^{(1,-1)} = 0.217$, $\kappa_{zc}^{(2,-1)} = 0.128$, and $\kappa_{zc}^{(1,-1)} = 0.337$. This result leads to a scale law for the position of the moiré rings in the tunneling regime

$$\begin{aligned} k_{zc}^{(1,-1)} &= 0.217\frac{F_0}{\omega}, \\ k_{zc}^{(2,-1)} &= 0.128\frac{F_0}{\omega}, \\ k_{zc}^{(1,-2)} &= 0.337\frac{F_0}{\omega}, \end{aligned} \tag{34}$$

where we have used $\vec{\kappa} = (\omega/F_0)\,\vec{k}$. This means that the position of the center of the moiré rings scales as the inverse of the Keldysh parameter γ^{-1}, which is observed in Fig. 6(b) in the tunneling regime ($\gamma < 1$). In the multiphoton regime ($\gamma > 1$), we see in Fig. 6(a) that the center of the moiré rings follows an approximate linear behavior with γ, i.e., $\kappa_{zc}^{(1,-1)} \simeq 0.214\gamma$, $\kappa_{zc}^{(2,-1)} \simeq 0.124\gamma$, and $\kappa_{zc}^{(1,-1)} \simeq 0.345\gamma$, which is consistent with the asymptotic values for the center of the moiré rings in the multiphoton limit ($\gamma \gg 1$), observed in Fig. 6(b). The proportionality coefficients were calculated as the average slope of curves in Fig. 6(a) between $\gamma = 3$ and 4. The approximate agreement between the asymptotic values for the center of the moiré fringes in the multiphoton limit and the coefficients of Eq. (34) in the tunneling regime deserve more investigation. As the position of the moiré structures depends strongly on the Keldysh parameter (Fig. 6), it is doubtful that they could survive the averaging over the focal volume of the laser. However, in the multiphoton regime ($\gamma \gtrsim 1$), the position of the center of the moiré does not vary significantly with the Keldysh parameter γ, and consequently, on the laser intensity. Therefore, for low intensity lasers, moiré could, in principle, survive the intensity averaging. On the other hand, experimentalists could measure the momentum map for an intensity I and then for a slightly higher intensity $I + \Delta I$ and perform the difference. This would be a way to measure intensity-non-averaged ionization probabilities, where the moiré patterns could survive.

IV. CONCLUSIONS

We have presented a study of interference effects observed in the direct ionization of atoms subject to multicycle laser pulses with wavelength in the range of the mid-infrared. In the framework of the SPA we describe the full differential electron momentum distribution and identify side rings calculated within the SFA and TDSE [28] as the moiré fringes due to the interplay between the intra- and intercycle interferences of electron trajectories in photoelectron 3D momentum distribution. A whole family of moiré fringes of varying visibility is characterized. An analytical expression for the moiré patterns within a Fourier analysis is presented showing an excellent agreement with the numerical calculations. The principal (secondary) side rings are centered along the parallel momentum axis ($k_\perp = 0$) with k_z values where the spacing of the intracycle pattern is equal to (multiple of or one over

a multiple of) the intercycle spacing. The position of the center of the side rings follows a scale law depending on the Keldysh parameter γ. Finally, we have discussed the possibility of experimetally observing the moiré patterns in the doubly differential momentum distribution.

ACKNOWLEDGMENTS

We thank X-M. Tong for sending the TDSE data of Fig. 1(b). This work was supported by CONICET PIP0386, PICT-2016-0296, and PICT-2014-2363 of ANPCyT (Argentina), and the University of Buenos Aires (UBACyT 20020130100477).

[1] K. C. Kulander, J. Cooper, and K. J. Schafer, Phys. Rev. A **51**, 561 (1995).
[2] G. G. Paulus, W. Nicklich, and H. Walther, Europhys. Lett. **27**, 267 (1994).
[3] M. Lewenstein, K. C. Kulander, K. J. Schafer, and P. H. Bucksbaum, Phys. Rev. A **51**, 1495 (1995).
[4] G. F. Gribakin and M. Y. Kuchiev, Phys. Rev. A **55**, 3760 (1997).
[5] G. G. Paulus, F. Zacher, H. Walther, A. Lohr, W. Becker, and M. Kleber, Phys. Rev. Lett. **80**, 484 (1998).
[6] W. Becker, F. Grasbon, R. Kopold, D. B. Milošević, G. G. Paulus, and H. Walther, Adv. At., Mol., Opt. Phys. **48**, 35 (2002).
[7] C. C. Chirila and R. M. Potvliege, Phys. Rev. A **71**, 021402 (2005).
[8] F. Lindner, M. G. Schätzel, H. Walther, A. Baltuška, E. Goulielmakis, F. Krausz, D. B. Milošević, D. Bauer, W. Becker, and G. G. Paulus, Phys. Rev. Lett. **95**, 040401 (2005).
[9] R. Gopal, K. Simeonidis, R. Moshammer, T. Ergler, M. Dürr, M. Kurka, K.-U. Kühnel, S. Tschuch, C.-D. Schröter, D. Bauer, J. Ullrich, A. Rudenko, O. Herrwerth, T. Uphues, M. Schultze, E. Goulielmakis, M. Uiberacker, M. Lezius, and M. F. Kling, Phys. Rev. Lett. **103**, 053001 (2009).
[10] D. G. Arbó, E. Persson, and J. Burgdörfer, Phys. Rev. A **74**, 063407 (2006).
[11] D. G. Arbó, S. Yoshida, E. Persson, K. I. Dimitriou, and J. Burgdörfer, Phys. Rev. Lett. **96**, 143003 (2006).
[12] T. Marchenko, H. G. Muller, K. J. Schafer, and M. J. J. Vrakking, J. Phys. B **43**, 095601 (2010).
[13] X. Xie, S. Roither, D. Kartashov, E. Persson, D. G. Arbó, L. Zhang, S. Gräfe, M. S. Schöffler, J. Burgdörfer, A. Baltuška, and M. Kitzler, Phys. Rev. Lett. **108**, 193004 (2012).
[14] R. Reichle, H. Helm, and I. Y. Kiyan, Phys. Rev. Lett. **87**, 243001 (2001).
[15] B. Bergues, Z. Ansari, D. Hanstorp, and I. Y. Kiyan, Phys. Rev. A **75**, 063415 (2007).
[16] S. Bivona, G. Bonanno, R. Burlon, D. Gurrera, and C. Leone, Phys. Rev. A **77**, 051404 (2008).
[17] D. G. Arbó, K. L. Ishikawa, E. Persson, and J. Burgdörfer, Nucl. Instrum. Methods Phys. Res., Sect. B **279**, 24 (2012).
[18] D. G. Arbó, K. L. Ishikawa, K. Schiessl, E. Persson, and J. Burgdörfer, Phys. Rev. A **81**, 021403 (2010).
[19] D. G. Arbó, K. L. Ishikawa, K. Schiessl, E. Persson, and J. Burgdörfer, Phys. Rev. A **82**, 043426 (2010).
[20] A. K. Kazansky and N. M. Kabachnik, J. Phys. B **43**, 035601 (2010).
[21] S. Bivona, G. Bonanno, R. Burlon, and C. Leone, Laser Phys. **20**, 2036 (2010).
[22] A. A. Gramajo, R. Della Picca, C. R. Garibotti, and D. G. Arbó, Phys. Rev. A **94**, 053404 (2016).
[23] A. A. Gramajo, R. Della Picca, and D. G. Arbó, Phys. Rev. A **96**, 023414 (2017).
[24] A. A. Gramajo, R. Della Picca, S. D. López, and D. G. Arbó, J. Phys. B **51**, 055603 (2018).
[25] P. Agostini, F. Fabre, G. Mainfray, G. Petite, and N. K. Rahman, Phys. Rev. Lett. **42**, 1127 (1979).
[26] M. Protopapas, C. H. Keitel, and P. L. Knight, Rep. Prog. Phys. **60**, 389 (1997).
[27] C. J. Joachain, M. Dörr, and N. Kylstra, Adv. At., Mol., Opt. Phys. **42**, 225 (2000).
[28] C. Lemell, J. Burgdörfer, S. Gräfe, K. I. Dimitriou, D. G. Arbó, and X.-M. Tong, Phys. Rev. A **87**, 013421 (2013).
[29] G. Lebanon and A. M. Bruckstein, *Energy Minimization Methods in Computer Vision and Pattern Recognition*, edited by M. Figueiredo, J. Zerubia, and A. Jain, Lecture Notes in Computer Science Vol. 2134 (Springer-Verlag, Berlin, Heidelberg, 2001), pp. 185–200.
[30] H. Miao, A. Panna, A. A. Gomella, E. E. Bennett, S. Znati, L. Chen, and H. Wen, Nat. Phys. **12**, 830 (2016).
[31] Lord Rayleigh, Phil. Mag., Ser. 4 **47**, 81 (1874).
[32] G. Oster and Y. Nishijima, Sci. Am. **208**, 54 (1963).
[33] G. Oster, M. Wasserman, and C. Zwerling, J. Opt. Soc. Am. **54**, 169 (1964).
[34] Y. Nishijima and G. Oster, J. Opt. Soc. Am. **54**, 1 (1964).
[35] P. A. Macri, J. E. Miraglia, and M. S. Gravielle, J. Opt. Soc. Am. B **20**, 1801 (2003).
[36] V. D. Rodríguez, E. Cormier, and R. Gayet, Phys. Rev. A **69**, 053402 (2004).
[37] M. Ivanov, P. B. Corkum, T. Zuo, and A. Bandrauk, Phys. Rev. Lett. **74**, 2933 (1995).
[38] S. Zhou, Y. Fu, X. Tang, S. Hu, W. Chen, and Y. Yang, Opt. Express **16**, 7869 (2008).
[39] D. P. Dewangan and J. Eichler, Phys. Rep. **247**, 59 (1994).
[40] D. Wolkow, Z. Phys. **94**, 250 (1935).
[41] D. G. Arbó, J. E. Miraglia, M. S. Gravielle, K. Schiessl, E. Persson, and J. Burgdörfer, Phys. Rev. A **77**, 013401 (2008).
[42] P. B. Corkum, N. H. Burnett, and M. Y. Ivanov, Opt. Lett. **19**, 1870 (1994).
[43] P. A. Korneev, S. V. Popruzhenko, S. P. Goreslavski, T.-M. Yan, D. Bauer, W. Becker, M. Kübel, M. F. Kling, C. Rödel, M. Wünsche, and G. G. Paulus, Phys. Rev. Lett. **108**, 223601 (2012).
[44] P. A. Korneev, S. V. Popruzhenko, S. P. Goreslavski, W. Becker, G. G. Paulus, B. Fetić, and D. B. Milošević, New J. Phys. **14**, 055019 (2012).
[45] F. H. M. Faisal and G. Schlegel, J. Phys. B **38**, L223 (2005).
[46] X.-M. Tong (private communication).
[47] D. G. Arbó, K. I. Dimitriou, E. Persson, and J. Burgdörfer, Phys. Rev. A **78**, 013406 (2008).